A seasonal algorithm of the snow-covered area fraction for mountainous terrain

Nora Helbig [1], Michael Schirmer [1], Jan Magnusson [2], Flavia Mäder [1,3], Alec van Herwijnen [1], Louis Quéno [1], Yves Bühler [1], Jeff S. Deems [4], and Simon Gascoin [5]

[1]WSL Institute for Snow and Avalanche Research SLF, Davos, Switzerland
[2]Statkraft AS, Oslo, Norway
[3]Institute of Geography, University of Bern, Bern, Switzerland
[4]National Snow and Ice Data Center, University of Colorado, Boulder, CO, USA
[5]Centre d'Etudes Spatiales de la Biosphère, CESBIO, Univ. Toulouse, CNES/CNRS/INRAE/IRD/UPS, 31401 Toulouse, France

Correspondence: Nora Helbig (norahelbig@gmail.com)

Abstract. The snow cover spatial variability in mountainous terrain changes considerably over the course of a snow season. In this context, fractional snow-covered area ($fSCA$) is an essential model parameter characterizing how much ground surface in a grid cell is currently covered by snow. We present a seasonal $fSCA$ algorithm using a recent scale-independent $fSCA$ parameterization. For the seasonal implementation, we track snow depth (HS) and snow water equivalent (SWE), and account for several alternating accumulation-ablation phases. Besides tracking HS and SWE, the seasonal $fSCA$ algorithm only requires subgrid terrain parameters from a fine-scale summer digital elevation model. We implemented the new algorithm in a multilayer energy balance snow cover model. To evaluate the spatiotemporal changes in modelled $fSCA$, we compiled three independent $fSCA$ data sets derived from airborne-acquired fine-scale HS data, as well as $fSCA$ data derived from satellite and terrestrial imagery. Overall, modelled daily 1km-$fSCA$ values had normalized root mean square errors of respectively 7 %, 12 % and 21 %, and some seasonal trends were identified. Comparing our algorithm performances to the performances of the CLM5.0 $fSCA$ algorithm implemented in the multilayer snow cover model demonstrated that our full seasonal $fSCA$ algorithm better represented seasonal trends. Overall, the results suggest that our seasonal $fSCA$ algorithm can be applied in other geographic regions by any snow model application.

1 Introduction

In mountainous terrain, the large spatial variability of the snow cover is driven by the interaction of meteorological variables with the underlying topography. Over the course of a winter season, the dominating topographic interactions with wind, precipitation and radiation vary considerably, generating characteristic seasonal dynamics of spatial snow depth variability (e.g. Luce et al., 1999). This spatial variability, or how much of the ground is actually covered by snow, is typically characterized by the fractional snow-covered area ($fSCA$). $fSCA$ is a crucial parameter in model applications such as weather forecasts (e.g. Douville et al., 1995; Doms et al., 2011), hydrological modelling (e.g. Luce et al., 1999; Thirel et al., 2013; Magnusson

et al., 2014; Griessinger et al., 2016, 2019) or avalanche forecasting (Bellaire and Jamieson, 2013; Horton and Jamieson, 2016; Vionnet et al., 2014), and is also used for climate scenarios (e.g. Roesch et al., 2001; Mudryk et al., 2020).

$fSCA$ can be retrieved from various satellite sensor images, including Moderate Resolution Imaging Spectroradiometer (MODIS) or Sentinel-2 (e.g. Hall et al., 1995; Painter et al., 2009; Drusch et al., 2012; Masson et al., 2018; Gascoin et al., 2019). Nevertheless, solutions are required to correct for temporal and spatial inconsistent coverage due to time gaps between satellite revisits, data delivery and the frequent presence of clouds (Parajka and Blöschl, 2006; Gascoin et al., 2015). Though fine-scale spatial snow cover models provide spatial snow depth distributions that could be used to derive coarse-scale $fSCA$, applying such models to larger regions is generally not feasible. This is in part due to computational cost, a lack of detailed input data and limitations in model structure or parameters. While some of these limitations can be overcome using current snow cover model advances applying data assimilation routines (e.g. Andreadis and Lettenmaier, 2006; Nagler et al., 2008; Thirel et al., 2013; Griessinger et al., 2016; Huang et al., 2017; Baba et al., 2018; Griessinger et al., 2019; Cluzet et al., 2020), the inherent uncertainties in input or assimilation data still remain. Computationally efficient subgrid $fSCA$ parameterizations, accounting for unresolved snow depth variability, are therefore still the method of choice for coarse-scale model systems, such as weather forecast, land surface and earth system models. Furthermore, $fSCA$ parameterizations are essential when assimilating satellite snow-covered area data in model systems (e.g. Zaitchik and Rodell, 2009)

Several compact, closed-form $fSCA$ parameterizations were suggested for coarse-scale model applications (e.g. Douville et al., 1995; Roesch et al., 2001; Yang et al., 1997; Niu and Yang, 2007; Su et al., 2008; Zaitchik and Rodell, 2009; Swenson and Lawrence, 2012). Most of these $fSCA$ parameterizations were heuristically developed. Some parameterizations introduced subgrid terrain parameters (e.g. Douville et al., 1995; Roesch et al., 2001; Swenson and Lawrence, 2012). The $tanh$-form, suggested by Yang et al. (1997), was later confirmed by integrating theoretical log-normal snow distributions and fitting the resulting parametric depletion curves using the spatial snow depth distribution (σ_{HS}) in the denominator of fitted $fSCA$ curves (Essery and Pomeroy, 2004). Through advances in remote sensing techniques, fine-scale spatial snow depth (HS) data became more readily available allowing to empirically parameterize σ_{HS} in complex topography at peak of winter (PoW) or during accumulation (Helbig et al., 2015b; Skaugen and Melvold, 2019). By parameterizing σ_{HS} using subgrid terrain parameters, Helbig et al. (2015b) expanded the $tanh$-$fSCA$ parameterization of Essery and Pomeroy (2004) to account for topographic influence. Recently, Helbig et al. (2021) re-evaluated this empirically derived $fSCA$ parameterization with high-resolution spatial HS sets from 7 different geographic regions at PoW, and made it applicable across spatial scales $\geq$ 200 m by introducing a scale-dependency in the dominant model descriptors.

Many studies highlighted that the same mean HS in early winter or in late spring can lead to substantially different $fSCA$ (Luce et al., 1999; Niu and Yang, 2007; Magand et al., 2014). This has led to the introduction of hysteresis in some $fSCA$ parameterizations (e.g. Luce et al., 1999; Swenson and Lawrence, 2012). Previously found interannual time-persistent correlations between topographic parameters and snow depth distributions (e.g. Schirmer et al., 2011; Schirmer and Lehning, 2011; Revuelto et al., 2014; López-Moreno et al., 2017) suggest indeed that a time-dependent $fSCA$ implementation might be feasible. However, a seasonal model implementation of a closed form $fSCA$ parameterization also needs to account for alternating snow accumulation and melt events during the season. Especially at lower elevations and increasingly so with climate change,

the separation of the depletion curve in only one accumulation period followed by a melting period is no longer applicable (e.g. Egli and Jonas, 2009). A seasonal $fSCA$ implementation in mountainous regions that accounts for these alternating periods is challenging. While some seasonal $fSCA$ implementations of varying complexities were previously proposed (e.g. Niu and Yang, 2007; Su et al., 2008; Egli and Jonas, 2009; Swenson and Lawrence, 2012; Nitta et al., 2014; Magnusson et al., 2014; Riboust et al., 2019) a detailed evaluation of seasonally parameterized $fSCA$ with $fSCA$ derived from high-resolution spatial and temporal HS data or snow products is currently still missing.

Here, we present a seasonal $fSCA$ implementation and evaluate it with high-resolution observation data in various geographic regions throughout Switzerland. The algorithm is based on the $fSCA$ parameterization for complex topography proposed by Helbig et al. (2015b, 2021). We apply two different empirical parameterizations for the spatial snow depth distribution, from Egli and Jonas (2009) and Helbig et al. (2021), with seasonal and current HS values to describe the hysteresis. Snow accumulation and melt events during the season are accounted for by tracking the history of HS and SWE values throughout the snow season. We implemented the algorithm in a multilayer energy balance snow cover model (modified JIM, the JULES investigation model by Essery et al. (2013)) which we ran with COSMO-1 (operated by MeteoSwiss) reanalysis data, measured HS and RhiresD precipitation data (MeteoSwiss). The seasonal performance of this algorithm was evaluated using $fSCA$ data sets from terrestrial cameras, airborne surveys and satellite imagery. This allowed us to assess modelled $fSCA$ using independent HS data sets with high spatial resolution and snow products with high temporal resolution. We further implemented the Community Land Model (CLM5.0) $fSCA$ algorithm accounting for hysteresis in accumulation and ablation (Lawrence et al., 2018), which is based on the work of Swenson and Lawrence (2012), in the multilayer energy balance snow cover model. Modelled $fSCA$ from the CLM5.0 $fSCA$ algorithm was also assessed with the measured $fSCA$ data sets and the performances compared to those of our seasonal $fSCA$ algorithm.

2 Fractional snow-covered area algorithm

In the following, we introduce the seasonal $fSCA$ algorithm in two parts. First we present the closed-form $fSCA$ parameterization derived by Helbig et al. (2015b). This formulation uses the spatial subgrid variability of snow depth (σ_{HS}) and snow depth HS of a grid cell. To derive σ_{HS}, we used two different statistical parameterizations. Second, we describe our seasonal $fSCA$ algorithm, i.e. how we handle the distinctly different paths between σ_{HS} and HS during accumulation and melt periods, i.e. the hysteresis.

2.1 $fSCA$ parameterization

The core of our seasonal algorithm is the PoW parameterization of Helbig et al. (2015b) relating $fSCA$ to HS and σ_{HS}:

$$fSCA = \tanh(1.3\,\frac{HS}{\sigma_{HS}})\,. \tag{1}$$

By including both HS and σ_{HS}, this formulation accounts for the close link between spatial subgrid snow depth variability and topography in $fSCA$. Although Eq. (1) was derived for PoW, in our seasonal $fSCA$ algorithm we apply it throughout the

3

entire snow season by using two different parameterizations for σ_{HS}, one accounting for subgrid topography (Helbig et al., 2021), while the second only depends on HS (Egli and Jonas, 2009).

σ_{HS} parameterization accounting for topography

90 We use the PoW subgrid parameterization for σ_{HS} in mountainous terrain originally developed by Helbig et al. (2015b) and later extended by Helbig et al. (2021). This parameterization accounts for the impact of topography on the spatial snow depth distribution at PoW:

$$\sigma_{HS}^{\text{Helbig}} = HS^c \mu^d \exp[-(\xi/L)^2] . \tag{2}$$

The parameterization contains two scale-dependent parameters c and d:

95
$$\begin{aligned} c &= 0.5330 \, L^{0.0389} \\ d &= 0.3193 \, L^{0.1034} . \end{aligned} \tag{3}$$

This σ_{HS} subgrid parameterization is generally valid for domain sizes (i.e. the coarse grid cell size) $L \geq 200$ m. Besides domain size L, Eq. (3) requires snow depth HS and subgrid summer terrain parameters μ and ξ. The mean squared slope related parameter $\mu = \left\{ \overline{[(\partial_x z)^2 + (\partial_y z)^2]/2} \right\}^{1/2}$ is derived using partial derivatives of subgrid terrain elevations z, i.e. from a summer digital elevation model (DEM). The correlation length $\xi = \sqrt{2}\sigma_z/\mu$ is derived for each L using the standard deviation

100 σ_z of terrain elevations z. The L/ξ-ratio in Eq. (3), describes the frequency of topographic features of length scale ξ in a domain L. All terrain parameters are derived on linearly detrended summer DEMs (Helbig et al., 2015b). More details on Eq. (2) and (3) can be found in Helbig et al. (2015b, 2021).

σ_{HS} parameterization not accounting for topography

The second σ_{HS} parameterization was developed by Egli and Jonas (2009) by fitting daily spatial HS means and standard

105 deviation of HS from 77 weather stations distributed throughout the Swiss Alps over six consecutive winter seasons during accumulation season. The resulting parameterization uses HS and a constant fit parameter:

$$\sigma_{HS}^{\text{Egli}} = HS^{0.839} . \tag{4}$$

This parameterization does not account for the impact of topography on σ_{HS}.

2.2 Seasonal $fSCA$ algorithm

110 To use the above $fSCA$ formulation (Eq. 1) throughout an entire snow season, we track changes in HS with time. This is done to account for the fact that after a snowfall, $fSCA$ can dramatically increase. Once the new snow has settled or started to melt, $fSCA$ values then generally return to similar values as before. We account for this by computing two $fSCA$ values in parallel, namely a seasonal $fSCA$ ($fSCA_{\text{season}}$) and a new snow $fSCA$ ($fSCA_{\text{nsnow}}$). $fSCA_{\text{season}}$ accounts for the entire history of the snow season up to the current time step, and thus all processes shaping the spatial snow depth distribution. It is therefore

computed using $\sigma_{HS}^{\text{Helbig}}$ (Eq. 3), which accounts for subgrid topography. $fSCA_{\text{nsnow}}$ only accounts for contributions by recent snowfall. As a snowfall generally covers most of the topography within a grid cell (i.e. all surfaces are initially covered by snow), we use $\sigma_{HS}^{\text{Egli}}$ (Eq. 4), which does not account for subgrid topography.

$fSCA_{\text{season}}$

To compute $fSCA_{\text{season}}$, we use extreme HS values at each time step per grid cell (Figure 1a). It is important to note that we identify these extremes using SWE rather than HS, as due to snow settlement HS values can peak even before a precipitation event has ended. However, as our $fSCA$ algorithm requires HS as input, we search for extreme SWE values in time, and use the corresponding HS values. In the following we will not specify this anymore, and only refer to extreme values of HS. To compute $fSCA_{\text{season}}$ we use $\sigma_{HS}^{\text{Helbig}}$ (Eq. 3) in the $fSCA$ formulation (Eq. 1) as follows:

$$fSCA_{\text{season}} = \tanh\left(1.3\,\frac{HS_{\text{pseudo-min}}}{\sigma_{HS_{\max}}^{\text{Helbig}}}\right) . \tag{5}$$

Here, $HS_{\text{pseudo-min}}$ is the current HS value or a recent minimum (pink dots in Figure 1a), and $\sigma_{HS_{\max}}^{\text{Helbig}}$ is computed using the current seasonal maximum snow depth $HS_{\max}$, i.e. the maximum in HS from the start of the season up to the current time step (green dots in Figure 1a). We call $HS_{\text{pseudo-min}}$ a pseudo-minimum as it is not the absolute seasonal minimum. At each time step, $HS_{\text{pseudo-min}}$ and $HS_{\max}$ are updated to compute $fSCA$. Note that after the PoW, $HS_{\max}$ and $\sigma_{HS_{\max}}^{\text{Helbig}}$ remain constant.

For the rare, completely flat grid cells, i.e. a subgrid mean slope angle of zero, Eq. (3) would always result in $fSCA = 1$. In those cases, we therefore use Eq. (4) instead of Eq. (3) to compute $fSCA_{\text{season}}$.

$fSCA_{\text{nsnow}}$

To account for possible increases in $fSCA$ after recent snowfalls, we evaluate $fSCA$ (Eq. 1) using $\sigma_{HS}^{\text{Egli}}$ (Eq. 4) computed with differences in snow depth dHS (only positive changes) within the last 14 days (Figure 1b). We use dHS rather than HS to only account for the contribution of new snow on changes in $fSCA$, thus as if the new snow fell on bare ground. A time window of 14 days provided reliable $fSCA$ results after intensive testing, but the length of this period may require further investigation once more is known about changes in snow depth distributions in mountainous terrain after snowfall.

Within the 14 day time window, we compute two different $fSCA$ values and then retain the maximum value. First, we evaluate $fSCA_{\text{nsnow}}^{\text{14day}}$ using the largest positive change in snow depth within the last 14 days:

$$fSCA_{\text{nsnow}}^{\text{14day}} = \tanh\left(1.3\,\frac{(HS_{\text{current}} - HS_{\min}^{\text{14day}})}{\sigma_{dHS^{\text{14day}}}^{\text{Egli}}}\right) . \tag{6}$$

Here, HS_{current} is the snow depth at the current time step (blue dot in Figure 1b), $HS_{\min}^{\text{14day}}$ is the minimum snow depth in the last 14 days (pink dot in Figure 1b), and $\sigma_{dHS^{\text{14day}}}^{\text{Egli}}$ is computed using the maximum difference in snow depth $dHS^{\text{14day}} = HS_{\max}^{\text{14day}} - HS_{\min}^{\text{14day}}$ in the last 14 days, with $HS_{\max}^{\text{14day}}$ the maximum snow depth in the last 14 days (green dot in Figure 1b).
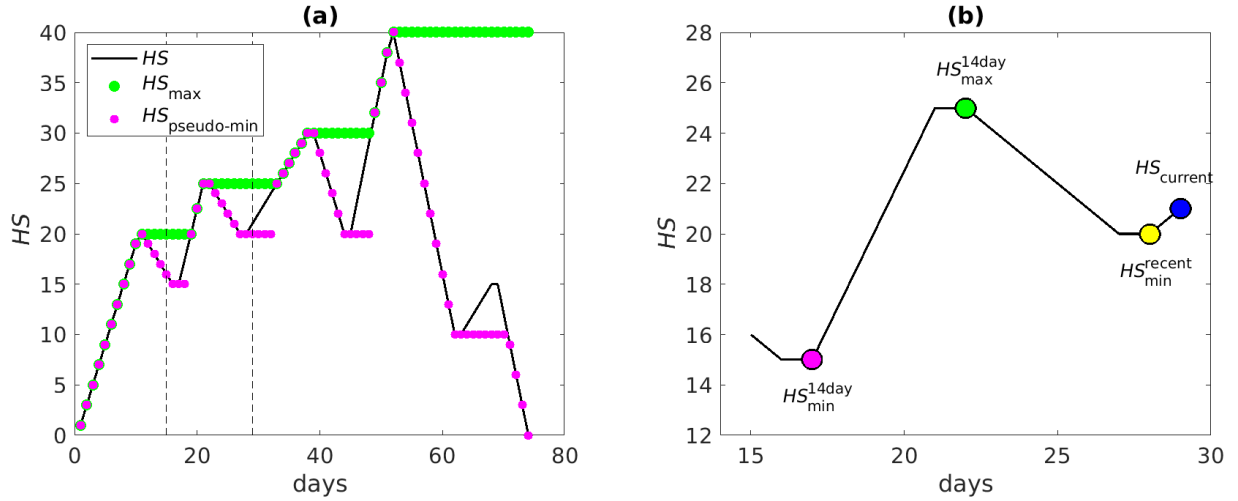
Figure 1. Schematic representation of snow depth HS extreme values used to compute $fSCA$ for a grid cell. (a) To determine $fSCA_{\text{season}}$, extremes in HS (black line) are tracked over the entire season. When HS decreases, the seasonal maximum snow depth HS_{max} (green dots) remains constant until a new maximum is reached with subsequent snowfalls. The pseudo-minimum $HS_{\text{pseudo-min}}$ (pink dots) decreases when HS decreases, until the next snowfall. It then remains constant until HS either exceeds HS_{max} or decreases below the previous minimum. (b) To determine $fSCA_{\text{nsnow}}$, several extremes in HS (black line) are tracked within the last 14 days (black dashed lines in a): the current value HS_{current} (blue dot), the minimum within the last 14 days $HS_{\text{min}}^{\text{14day}}$ (pink dot), the maximum within the last 14 days $HS_{\text{max}}^{\text{14day}}$ (green dot), and the minimum prior to the most recent snowfall $HS_{\text{min}}^{\text{recent}}$ (yellow dot).

Second, we evaluate $fSCA_{\text{nsnow}}^{\text{recent}}$ using only the most recent change in snow depth within the last 14 days:

$$fSCA_{\text{nsnow}}^{\text{recent}} = \tanh\left(1.3\, \frac{dHS^{\text{recent}}}{\sigma_{dHS^{\text{recent}}}^{\text{Egli}}}\right). \tag{7}$$

145 Here, $dHS^{\text{recent}} = HS_{\text{current}} - HS_{\text{min}}^{\text{recent}}$ is the change in snow since the most recent snowfall, where $HS_{\text{min}}^{\text{recent}}$ is the minimum snow depth prior to the snowfall (yellow dot in Figure 1b). $fSCA_{\text{nsnow}}^{\text{recent}}$ avoids spatial discontinuities: Without this implementation, grid cells with $HS > 0$ m prior to a recent snowfall may have a lower $fSCA$ value than grid cells where the same amount of new snow has fallen on the bare ground.

Finally, the maximum of $fSCA_{\text{nsnow}}^{\text{14day}}$ and $fSCA_{\text{nsnow}}^{\text{recent}}$ gives $fSCA_{\text{nsnow}}$ for the current time step and a grid cell.

150 **Seasonal algorithm**

Over the course of the snow season, we derive $fSCA_{\text{nsnow}}$ and $fSCA_{\text{season}}$ for each time step and grid cell (Figure 2). The final $fSCA$ was then obtained by taking the maximum of both values. This full seasonal $fSCA$ algorithm, i.e. including the tracking of HS and SWE, was implemented in a distributed snow cover model. The code is publicly available on the
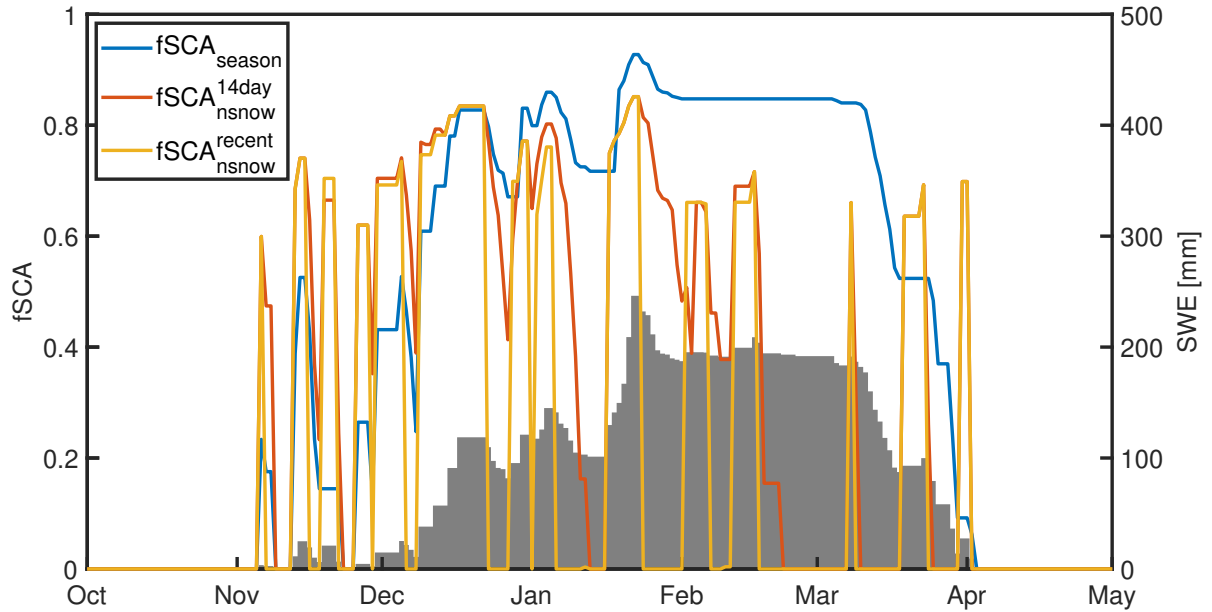
Figure 2. Illustration of modelled $fSCA_{nsnow}^{recent}$, $fSCA_{nsnow}^{14day}$ and $fSCA_{season}$ for one grid cell over a season. $fSCA$ is the maximum for each time step from $fSCA_{nsnow}$=max($fSCA_{nsnow}^{recent}$,$fSCA_{nsnow}^{14day}$) and $fSCA_{season}$. All terms are described in Section 2.2.

Table 1. Details of the different $fSCA$ algorithms that are compared to the full $fSCA$ algorithm in JIM$_{OSHD}$.

algorithm name	$fSCA_{season}$	$fSCA_{nsnow}$	tracking HS & SWE (Section 2.2)
JIM$_{OSHD}$	Eq. (5)	Eq. (6) & (7)	season & 14 days
JIM$_{OSHD}^{season}$	Eq. (5)	-	season
JIM$_{OSHD}^{curr}$	$\tanh\left(1.3\frac{HS_{current}}{\sigma_{HS_{current}}^{Helbig}}\right)$	-	-
JIM$_{OSHD}^{allHelbig}$	Eq. (5)	Eq. (6) & (7) with σ_{HS}^{Helbig}	season & 14 days
JIM$_{OSHD}^{Swenson*}$	Eq. (8.2) in	Eq. (8.1) in	season & 14 days
	Lawrence et al. (2018)	Lawrence et al. (2018)	

WSL/SLF GitLab repository (cf. Code availability section). The data sets used to evaluate the performance of this algorithm
155 are described in the next section.

3 Data

3.1 Modelled $fSCA$ and HS maps

We model the snow cover evolution using the JULES investigation model (JIM). JIM is a multi-model framework of physically based energy-balance models solving the mass and energy balance for a maximum of three snow layers (Essery, 2013). While the multi-model framework JIM offers 1701 combinations of various process parameterizations, Magnusson et al. (2015) selected a specific combination that performed best for snow melt modelling for Switzerland. The latter model combination is used to predict daily snow mass and snowpack runoff for the operational snow hydrology service (OSHD) at WSL Institute of Snow and Avalanche Research SLF. We ran JIM$_{\text{OSHD}}$ in 1 km resolution with hourly meteorological data from the COSMO-1 model (operated by MeteoSwiss) for Switzerland. We used a reanalysis product of daily observed precipitation (RhiresD) from MeteoSwiss as well as COSMO-1 data. Daily HS measurements from manual observers as well as from a dense network of automatic weather stations (AWS) were used to correct precipitation data via optimal interpolation (OI) (Magnusson et al., 2014), which is a computational efficient data assimilation approach. Using OI in JIM$_{\text{OSHD}}$, Griessinger et al. (2019) obtained improved discharge simulations in 25 catchments over four hydrological years.

To describe the subgrid snow cover evolution in mountainous terrain, our seasonal $fSCA$ algorithm was implemented in JIM$_{\text{OSHD}}$. As daily values, we used model output generated at 6 am (UTC). In the following, modelled $fSCA$ and HS maps refer to daily $fSCA$ and HS from JIM$_{\text{OSHD}}$ model output.

We also computed the snow cover evolution using JIM$_{\text{OSHD}}$ with various simplifications in the seasonal $fSCA$ algorithm as well as with the $fSCA$ parameterizations implemented in CLM5.0 (Lawrence et al., 2018) which are based on Swenson and Lawrence (2012) (cf. Table 1 for more details). This latter $fSCA$ algorithm also accounts for hysteresis in accumulation and ablation by using two different $fSCA$ parameterizations and by tracking the seasonal maximum SWE. While subgrid topography is accounted for in the $fSCA$ parameterization during ablation via σ_z, topography is not accounted for during snowfall events. The algorithm of Swenson and Lawrence (2012) was derived by linking daily satellite-retrieved $fSCA$ to snow data. We implemented this algorithm in JIM using our snow tracking algorithm, i.e. the corresponding HS values such as $HS_{\text{pseudo-min}}$ (cf. Section 2.2). This was done to solely evaluate the differences in the $fSCA$ parameterizations. In total, we performed four additional snow cover simulations: JIM$_{\text{OSHD}}^{\text{season}}$, JIM$_{\text{OSHD}}^{\text{curr}}$, JIM$_{\text{OSHD}}^{\text{allHelbig}}$ and JIM$_{\text{OSHD}}^{\text{Swenson*}}$ (cf. Table 1).

3.2 Evaluation data

3.2.1 ADS fine-scale HS maps

We used fine-scale spatial HS maps gathered by airborne digital scanning (ADS) with an opto-electronic line scanner on an airplane. Data were acquired over the Wannengrat and Dischma area near Davos in the eastern Swiss Alps during winter and summer (Bühler et al., 2015). We used ADS-derived HS maps at three points in time during one winter season, namely during accumulation on 26 January ('acc'), at approximate peak of winter on 9 March ('PoW') and during ablation season on 20 April 2016 ('abl') (Marty et al., 2019). We used a summer DEM from ADS to derive the snow-free terrain parameters.

Each ADS data set covers about 150 km^2 with 2 m spatial resolution. Compared to terrestrial laser scan (TLS)-derived HS data, the 2 m ADS-derived HS maps had a root mean square error (RMSE) of 33 cm and a normalized median absolute deviation (NMAD) of 24 cm (Bühler et al., 2015).

3.2.2 ALS fine-scale HS maps

We used fine-scale spatial HS maps gathered by airborne laser scanning (ALS). The ALS campaign was a Swiss partner mission of the Airborne Snow Observatory (ASO) (Painter et al., 2016). Lidar setup and processing standards were similar to those in the ASO campaigns in California. Data were acquired over the Dischma area near Davos in the eastern Swiss Alps (cf. Figure 3a in Helbig et al., 2021). We used ALS-derived HS maps at three points in time during one winter season, namely at the approximate peak of winter on 20 March ('PoW') and during the early and late-ablation season on 31 March and 17 May 2017 ('abl'), respectively. We used a summer DEM from ALS from 29 August 2017 to derive the snow-free terrain parameters.

Each ALS data set covered about 260 km^2. The original 3 m resolution was aggregated to 5 m horizontal resolution. Comparing the ALS-derived HS data to manual snow probing within forest but outside canopy (i.e. not below a tree), Mazzotti et al. (2019) reported a RMSE of 13 cm and a bias of -5 cm for 20 March 2017.

3.2.3 Terrestrial camera images

We used camera images from terrestrial time-lapse photography in the visible band. The camera (Nikon Coolpix 5900 from 2016 to 2018, Canon EOS 400D from 2019 to 2020) was installed at the SLF/WSL in Davos Dorf in the eastern Swiss Alps (van Herwijnen and Schweizer, 2011; van Herwijnen et al., 2013). Photographs were taken of the Dorfberg in Davos, which is a large southeast-facing slope with a mean slope angle of about 30° (cf. Figure 1 in Helbig et al., 2015a). To obtain $fSCA$ values from the camera images, we followed the workflow described by Portenier et al. (2020). We used the algorithm of Salvatori et al. (2011) to classify pixels in the images as snow or snow-free. Though images are taken at regular intervals (between 2 and 15 minutes, depending on the year), we used the image at noon to derive $fSCA$ for that day. We evaluated images from five winter seasons (2016, 2017, 2018, 2019 and 2020) every time from 1 November to 30 June.

The resulting snow/no-snow map of the camera images had a horizontal resolution of 2 m. The field of view (FOV) overlaps with four 1 x 1 km JIM$_\text{OSHD}$ grid cells with projected visible fractions between 9 to 40 % in each grid cell. The camera FOV covers about 0.76 km^2.

3.2.4 Sentinel-2 snow products

We used fine-scale snow-covered area maps obtained from the Theia snow collection (Gascoin et al., 2019). The satellite snow products were generated from Sentinel-2 L2A and L2B images. We used Sentinel-2 snow-covered area maps over one winter season from 20 December 2017 to 31 August 2018 for Switzerland. We further used Sentinel-2 snow maps over the Dischma area near Davos close to or at the date of the three ALS-scans (18 and 28 March and 17 May 2017) and over the Dorfberg area in Davos Dorf from 1 November 2017 to 30 June 2018.

9
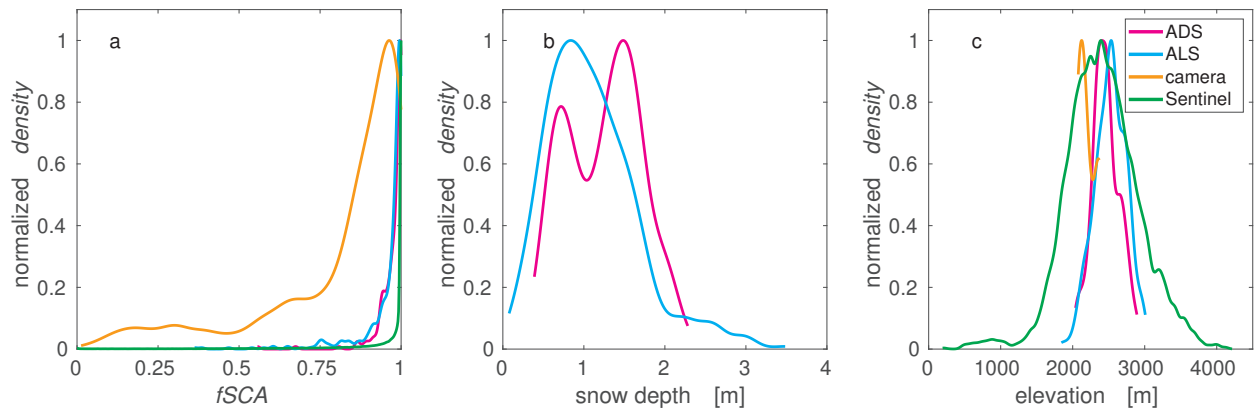
Figure 3. Probability density functions after preprocessing for all valid 1 km (a) $fSCA$, (b) snow depth and (c) elevation per measurement data set. All densities were normalized with the maximum in each data set. Colors represent the different measurement platforms as detailed in Section 3.2.

The horizontal resolution of the snow product is 20 m. While the spatial coverage of the Sentinel-2 snow-covered area maps in Switzerland varies every time step, Sentinel-2 may cover several thousand square kilometers. A validation of the Theia snow product with snow depth from AWS, through comparison to snow maps with higher spatial resolution as well as by visual inspection indicated that snow is well detected, although there is a tendency to underdetect snow (Gascoin et al., 2019). The main difficulty of satellite snow products is to avoid false snow detection within clouds. Furthermore, snow omission errors may occur on steep, shaded slopes when the solar elevation is typically below 20°.

3.3 Derivation of 1 km $fSCA$ evaluation data

For pre-processing, we masked out forest, rivers, glaciers or buildings in all fine-scale measurement data sets. Optical snow products that were obscured by clouds were also neglected. In all fine-scale HS data sets, we neglected HS values that were lower than zero or above 15 m. We used a HS threshold of zero m to decide whether or not a 2 or 5 m grid cell was snow-covered. This threshold could not be better adjusted due to a lack of independent observations.

We then aggregated all fine-scale snow data, as well as the snow products from optical imagery, in squared domain sizes L in regular grids of 1 km aligned with the OSHD model domain. For the spatial averages, we required at least 70 % valid data for the fine-scale snow data and at least 50 % valid for the satellite-derived $fSCA$ data in each 1 km grid cell. We excluded 1 km grid cells with spatial mean slope angles larger than 60° and spatial mean measured or modelled HS <5 cm. We further neglected 1 km grid cells with forest fractions larger than 10 %, derived from 25 m forest cover data. Overall, this led to a variable number of 1 km valid grid cells for the different data sets (Table 2). For the fine-scale snow data sets, this number ranged from 69 to 157 with a total of 668 valid 1 km grid cells. After cloud and forest removal, on average, every second day we had some valid Sentinel-2 data in Switzerland (153 valid days from the 255 calendar days). For the time period from 20 December 2017 to 31 August 2018, this resulted in 216'896 valid 1 km grid cells from a total of 2'274'991 valid OSHD

10

Table 2. Details of the valid 1 km $fSCA$ evaluation data sets after pre-processing as described in Section 3.3.

geographical region	remote sensing method	spatial coverage	temporal coverage	σ_{fSCA}	mean $fSCA$
		[km^2]	[days]		
Wannengrat and Dischma area (eastern CH)	ADS	232	3	0.05	0.98
Dischma and Engadin area (eastern CH)	ALS	436	3	0.08	0.96
Davos Dorfberg (eastern CH)	Terrestrial camera	931	337	0.23	0.81
Switzerland	Sentinel-2	216'896	153	0.18	0.93

grid cells in Switzerland, i.e. about 9.5 %. These valid 1 km grid cells covered terrain elevations from 174 m to 4278 m, subgrid mean slope angles from 0° to 60° and all terrain aspects. We used three of the four grid cells covered by the FOV of the terrestrial camera, since one grid cell had a forest fraction larger than 10 %. On average, every fourth day we had valid camera data (337 valid days from the 1212 calendar days). Valid camera-derived $fSCA$ for five seasons and the three grid cells covered by the FOV resulted in 931 valid 1 km grid cells from a total of 3'018 valid OSHD grid cells, i.e. 31 %. The three grid cells have terrain elevations of 2077 m, 2168 m and 2367 m and slope angles of 27°, 34° and 39°. The diversity in each of the evaluation data sets after pre-processing is indicated in Table 2 and is also shown for valid 1 km domains by means of the pdf for $fSCA$, HS and terrain elevation z in Figure 3.

3.4 Performance measures

To evaluate the performance of modelled $fSCA$ compared to the measurements, we used three measures: the root mean square error (RMSE), the normalized root mean square error (NRMSE; normalized by the mean of the measurements) and the mean percentage error (MPE; defined as measured minus modelled, normalized with the mean of the measurements).

4 Results

We present the evaluation of our seasonal $fSCA$ algorithm in three sections: evaluation with $fSCA$ derived from fine-scale HS maps near Davos, evaluation with $fSCA$ from time-lapse photography in Davos Dorf and evaluation with $fSCA$ from Sentinel-2 snow products over Switzerland. We further present some additional comparisons with Sentinel-2 snow products in the first two sections when Sentinel-2 data was available in the Davos area (cf. Section 3.2.4).

### 4.1 Evaluation with $fSCA$ from fine-scale HS maps

Modelled $fSCA$ compared well with $fSCA$ derived from all six fine-scale HS data sets. Overall, we obtained a NRMSE of 7 %, a RMSE of 0.07 and a MPE of 0.7 % (Table 3). The best performance was for the two dates at the approximate PoW

Table 3. Performance measures for modelled $fSCA$ with (I) $fSCA$ derived from all fine-scale HS maps (combined ADS- and ALS-derived $fSCA$) and (II) Sentinel-derived $fSCA$ (only available for ALS dates). Additionally, performance measures are shown for ALS-derived $fSCA$ with Sentinel-derived $fSCA$ (III) and for modelled $fSCA$ using $JIM_{OSHD}^{Swenson*}$ (IV). Given statistics are NRMSE, RMSE and MPE. For all differences we computed measured minus modelled values respectively Sentinel-derived $fSCA$ minus ALS-derived $fSCA$ for III. The different points in time of the season are specified in Section 3.2.

$fSCA$	NRMSE	RMSE	MPE
	[%]		[%]
I JIM_{OSHD} vs ADS&ALS			
all dates	7	0.07	0.7
accumulation date	8	0.08	-3.8
PoW dates	2	0.02	0.3
ablation dates	8	0.08	1.8
II JIM_{OSHD} vs Sentinel-2 (at ALS dates)			
all dates	9	0.08	-1.4
PoW dates	3	0.03	2.5
ablation dates	9	0.08	-1.5
III Sentinel-2 vs ALS			
all dates	11	0.10	3.1
PoW date	9	0.08	-5.9
ablation dates	11	0.10	3.4
IV $JIM_{OSHD}^{Swenson*}$ vs ADS&ALS			
all dates	14	0.14	-1.2
accumulation date	9	0.09	-6.1
PoW dates	6	0.06	-0.6
ablation dates	18	0.18	-0.7

(NRMSE of 2 %, a RMSE of 0.02 and a MPE of 0.3 %), while the performance was somewhat lower during the ablation and
260   accumulation period.

To investigate the influence of elevation, we binned the data in 200 m elevation bands for the ADS and ALS data sets separately (Figures 4 and 5). For ADS data, elevation-dependent modelled $fSCA$ values were comparable to the measurements at PoW and early ablation, while the differences during accumulation were more pronounced (compare red and black dots in Figure 4). There was also no consistent elevation trend, as during accumulation differences between modelled and measured
265   $fSCA$ increased with elevation, while during early ablation the opposite was true. For the ALS data, measurements were only available at PoW and during ablation. Overall, modelled $fSCA$ values were again in line with the measurements (compare red and black dots in Figure 5). The largest difference was observed for the lowest elevation bin (0.15 at PoW at 1800m; Figure
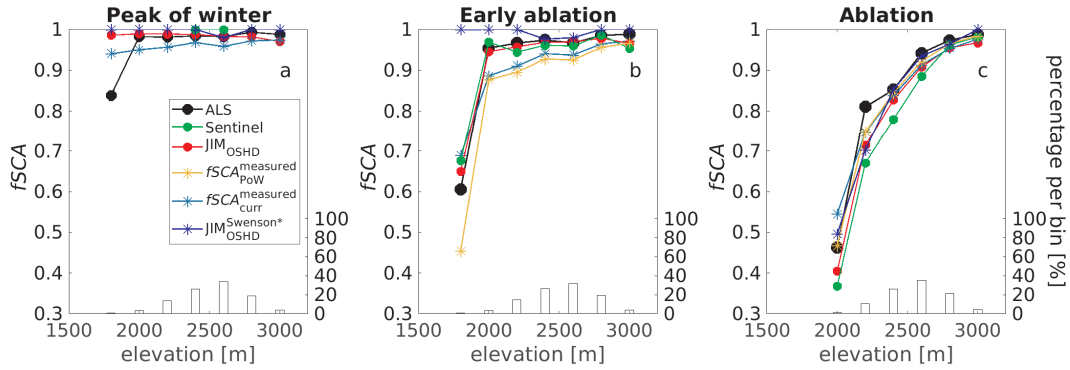
12
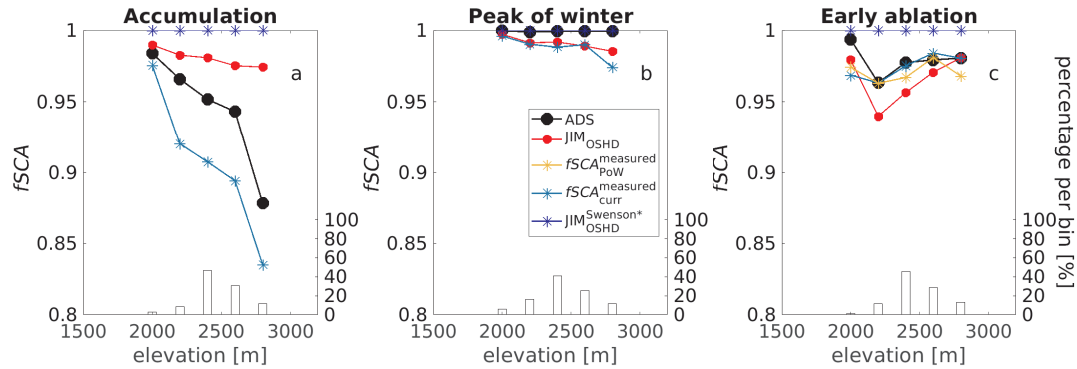
Figure 4. Modelled and ADS-derived $fSCA$ in 200 m elevation bins for three dates: (a) during accumulation, (b) at approximate peak of winter (PoW), and (c) during ablation. Two benchmarks based on Eq. (1) are shown where applicable: $fSCA_{\mathrm{PoW}}^{\mathrm{measured}}$ (orange stars) uses HS form the current ADS scan and σ_{HS} from the ADS scan at PoW, while $fSCA_{\mathrm{curr}}^{\mathrm{measured}}$ (light blue stars) uses HS and σ_{HS} form the current ADS scan. The bars show the valid data percentage per bin.

5a), and for the late ablation data, modelled $fSCA$ was consistently lower than ALS-derived $fSCA$, in particular for the lower elevation bins (Figure 5c).

Valid Sentinel-2 data were only available on dates close to the ALS measurements (green dots in Figure 5), not to the ADS measurement dates. Overall, modelled and Sentinel-derived $fSCA$ values were in good agreement for the three ALS dates (II in Table 3), there was no clear elevation dependence (compare green and red dots in Figure 5), and differences were at most 0.05 (for elevations between 2300 m and 2500 m in Figure 5c). The Sentinel-derived $fSCA$ values can also be compared to those from the ALS scans. In this case, the performance measures were somewhat lower (compare II and III in Table 3), and Sentinel-derived $fSCA$ values were especially lower than the ALS data in late ablation (compare green and black dots in Figure 5c).

Our seasonal $fSCA$ algorithm is implemented in a complex operational snow cover model framework (Section 3.1). Uncertainties related to input or model structure therefore impact modelled HS and $fSCA$ values. To investigate the influence of these uncertainties more closely, we also derived two benchmark $fSCA$ models based on Eq. (1) using measured rather than modelled HS data. The first benchmark $fSCA_{\mathrm{curr}}^{\mathrm{measured}}$ (light blue stars in Figures 4 and 5) uses measured HS and σ_{HS} from the current scan. The second benchmark $fSCA_{\mathrm{PoW}}^{\mathrm{measured}}$ (orange stars in Figures 4 and 5) combines current HS measurements with σ_{HS} values measured at PoW. At PoW, $fSCA_{\mathrm{PoW}}^{\mathrm{measured}}$ and $fSCA_{\mathrm{curr}}^{\mathrm{measured}}$ are the same, and $fSCA_{\mathrm{PoW}}^{\mathrm{measured}}$ can only be derived at or after PoW. Results obtained with both benchmark models were similar, except for the lowest elevation bin in the ALS data set (Figure 5b and c). Overall, the values of $fSCA_{\mathrm{curr}}^{\mathrm{measured}}$ were somewhat closer to the measured $fSCA$ values (e.g. Figure 4c or 5b). Both benchmark models were closest to the measured $fSCA$ values during the ablation season (Figure 4c and 5c), and overall the agreement was better for higher elevation bins. Our seasonal $fSCA$ implementation (red dots in Figures 4 and 5) was also similar to both benchmark models. The largest differences were during the accumulation period (Figure 4a).
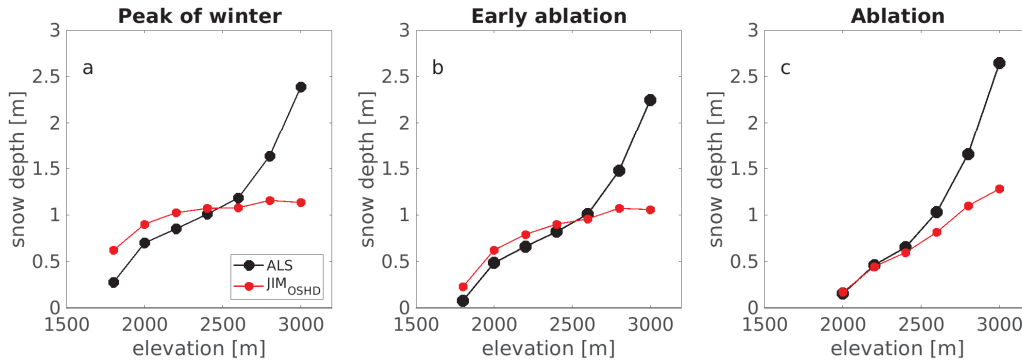
Figure 5. Modelled and ALS-derived, and Sentinel-derived $fSCA$ in 200 m elevation bins for three dates: (a) at approximate PoW, (b) during early ablation and (c) during late ablation. The same two benchmarks based on Eq. (1) as in Figure 4 are also shown where applicable. Sentinel-derived $fSCA$ (green dots) was available 2 days before the PoW scan, 3 days before the early ablation scan and on the same day as the late ablation scan. The bars show the valid data percentage per bin.
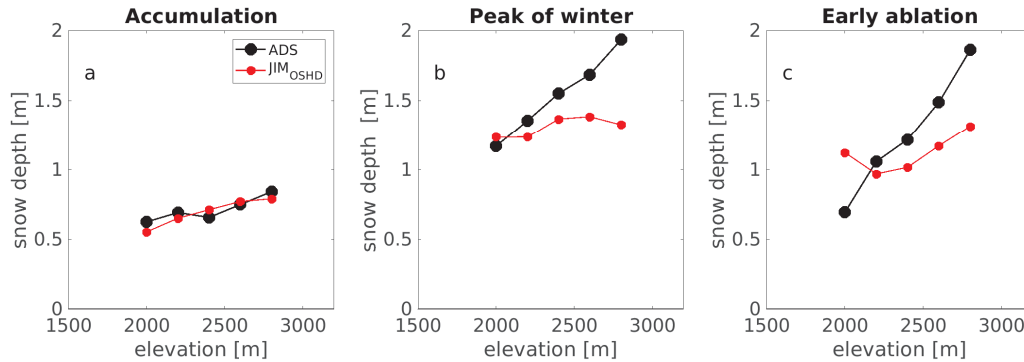
Figure 6. Modelled and ADS-derived HS in 200 m elevation bins for three dates: (a) during accumulation, (b) at approximate PoW and (c) during ablation.

As a final benchmark, we also compared our seasonal $fSCA$ implementation with the parameterizations implemented in CLM5.0 (cf. Table 1). Modelled $fSCA$ using JIM$_{OSHD}$ performed better than that modelled with JIM$_{OSHD}^{Swenson*}$ (compare I and IV in Table 3). During most of the season, $fSCA$ values from JIM$_{OSHD}^{Swenson*}$ were close to 1 and showed little elevation dependence (blue stars in Figure 4 and 5). The only exception was during the late-ablation season, when $fSCA$ from JIM$_{OSHD}$ and from JIM$_{OSHD}^{Swenson*}$ were very similar (blue and red dots in Figure 5c).

To investigate the origin of the discrepancies between modelled and observed $fSCA$ values more closely, we compared modelled and measured HS in 200 m elevation bins for the ADS and ALS data sets separately (Figure 6 and 7). For both data sets, modelled HS was substantially lower than measured HS at higher elevations. The only exception was for the accumulation date, when modelled and measured HS were in good agreement for all elevations (Figure 6a). For all dates and

14

Figure 7. Modelled and ALS-derived HS in 200 m elevation bins for three dates: (a) at approximate PoW, (b) during early ablation and (c) during ablation.

data sets, the NRMSE between modelled and measured HS was 12 % and the MPE was 14 %. Note that seasonal variations in ALS-HS across all elevations were generally much lower than those in the ADS-HS data. This was in part because the time intervals between the three ALS scans (20 March, 31 March, 17 May 2017) were shorter than for the ADS scans (26 January, 9 March and 20 April 2016), and there were also some snowfall events during the ALS ablation period (spring 2017).

4.2 Evaluation with $fSCA$ from camera images

The high temporal resolution of camera-derived $fSCA$ allowed us to evaluate the seasonal model performance. The seasonal trend in modelled $fSCA$ using JIM$_{OSHD}$ was generally in line with that from camera-derived $fSCA$ (compare red and black dots in Figure 8). For the grid cell at 2168 m, however, the agreement was somewhat poorer, as there was a delay in the modelled start of the ablation season, and modelled $fSCA$ values were too high during accumulation (Figure 8b,e).

For all winter seasons (2016 to 2020) and for the three grid cells, we obtained a NRMSE of 21 %, a RMSE of 0.17 and a MPE of -7 % (I in Table 4). Note that the inter-annual performance varied substantially, as did the performance among the three grid cells. For instance, for all three grid cells, the overall best performance was for the season 2018 (NRMSE = 14 %, RMSE = 0.11, MPE = -4 %), while the worst performance was for the season 2019 (NRMSE = 25 %, RMSE = 0.2, MPE = -12 %).

For winter season 2018, we used Sentinel-derived $fSCA$ to evaluate modelled and camera-derived $fSCA$ values. While overall the agreement between modelled and Sentinel-derived $fSCA$ was good (NRMSE 2 % and MPE of 1 %), the agreement between camera- and Sentinel-derived $fSCA$ was poorer (NRMSE = 12 %, MPE = 5 %). The latter performance values were however comparable to the agreement between modelled and camera-derived $fSCA$ for days with valid Sentinel-derived data (NRMSE = 12 %, MPE = -4 %).

The camera-derived $fSCA$ was also used to evaluate the relevance of applying our full seasonal $fSCA$ algorithm, as opposed to simplifications and JIM$_{OSHD}^{Swenson*}$ (cf. Table 1 for details). While overall $fSCA$ from JIM$_{OSHD}^{season}$ and JIM$_{OSHD}$ agreed well, there were substantial differences after snowfall events on partly snow-free ground (compare orange stars and red dots

15

Table 4. Performance measures for (I) modelled $fSCA$ using JIM_{OSHD} and camera-retrieved $fSCA$ for the winter seasons 2016 to 2020, (II) modelled $fSCA$ using JIM_{OSHD} and Sentinel-derived $fSCA$ for the three grid cells for the winter season 2018, (III) camera-derived $fSCA$ with Sentinel-derived $fSCA$ for the three grid cells, and (IV to VII) for all JIM modelled $fSCA$ versions (for details see Table 1), namely for $\text{JIM}_{\text{OSHD}}^{\text{season}}$, $\text{JIM}_{\text{OSHD}}^{\text{curr}}$, $\text{JIM}_{\text{OSHD}}^{\text{allHelbig}}$ and $\text{JIM}_{\text{OSHD}}^{\text{Swenson*}}$, with camera-derived $fSCA$.

$fSCA$	NRMSE	RMSE	MPE
	[%]		[%]
I JIM_{OSHD} vs camera			
	21	0.17	-7.1
II JIM_{OSHD} vs Sentinel-2			
	2	0.02	0.8
III camera vs Sentinel-2			
	12	0.11	5.0
IV $\text{JIM}_{\text{OSHD}}^{\text{season}}$ vs camera			
	22	0.18	-6.1
V $\text{JIM}_{\text{OSHD}}^{\text{curr}}$ vs camera			
	26	0.21	-9.2
VI $\text{JIM}_{\text{OSHD}}^{\text{allHelbig}}$ vs camera			
	21	0.17	-7.6
VII $\text{JIM}_{\text{OSHD}}^{\text{Swenson*}}$ vs camera			
	30	0.25	-10.6

in Figure 8). Specifically, after such a snowfall event, modelled $fSCA$ using JIM_{OSHD} generally increased, while $\text{JIM}_{\text{OSHD}}^{\text{season}}$ remained constant. Using $\text{JIM}_{\text{OSHD}}^{\text{curr}}$, modelled $fSCA$ values were less in line with those from JIM_{OSHD} (compare light blue stars and red dots in Figure 8). While discrepancies were again large after snowfall event, they were also pronounced during the ablation periods. In general, with $\text{JIM}_{\text{OSHD}}^{\text{curr}}$ the ablation season started later and was followed by a much steeper melt out period. Using $\text{JIM}_{\text{OSHD}}^{\text{curr}}$ can result in a substantially shorter snow season compared to JIM_{OSHD}, with a maximum difference of 21 days at 2168 m in the season 2017. Overall, compared to camera-derived $fSCA$, both simplified models performed less well than JIM_{OSHD} (Table 4). The performance using $\text{JIM}_{\text{OSHD}}^{\text{allHelbig}}$ was very similar to $fSCA$ from JIM_{OSHD}, i.e. applying $\sigma_{HS}^{\text{Helbig}}$ instead of $\sigma_{HS}^{\text{Egli}}$ for $fSCA_{\text{nsnow}}$ did not substantially affect model performance. On the contrary, $fSCA$ from $\text{JIM}_{\text{OSHD}}^{\text{Swenson*}}$ had the worse overall performances when compared to camera-derived $fSCA$ (VII in Table 4). Similar to $\text{JIM}_{\text{OSHD}}^{\text{curr}}$, using $\text{JIM}_{\text{OSHD}}^{\text{Swenson*}}$ considerably delayed the ablation season, followed by a much steeper melt out. The snow season was substantially shortened again by at most 32 days in the 2017 season at 2077 m. Modelled $fSCA$ using $\text{JIM}_{\text{OSHD}}^{\text{Swenson*}}$ also largely overestimates $fSCA$ during the accumulation period (blue dots in Figure 8). Overall, using $\text{JIM}_{\text{OSHD}}^{\text{Swenson*}}$ led to much steeper increases and decreases in $fSCA$, i.e. an almost binary seasonal $fSCA$ trend that was not in line with camera-derived $fSCA$.
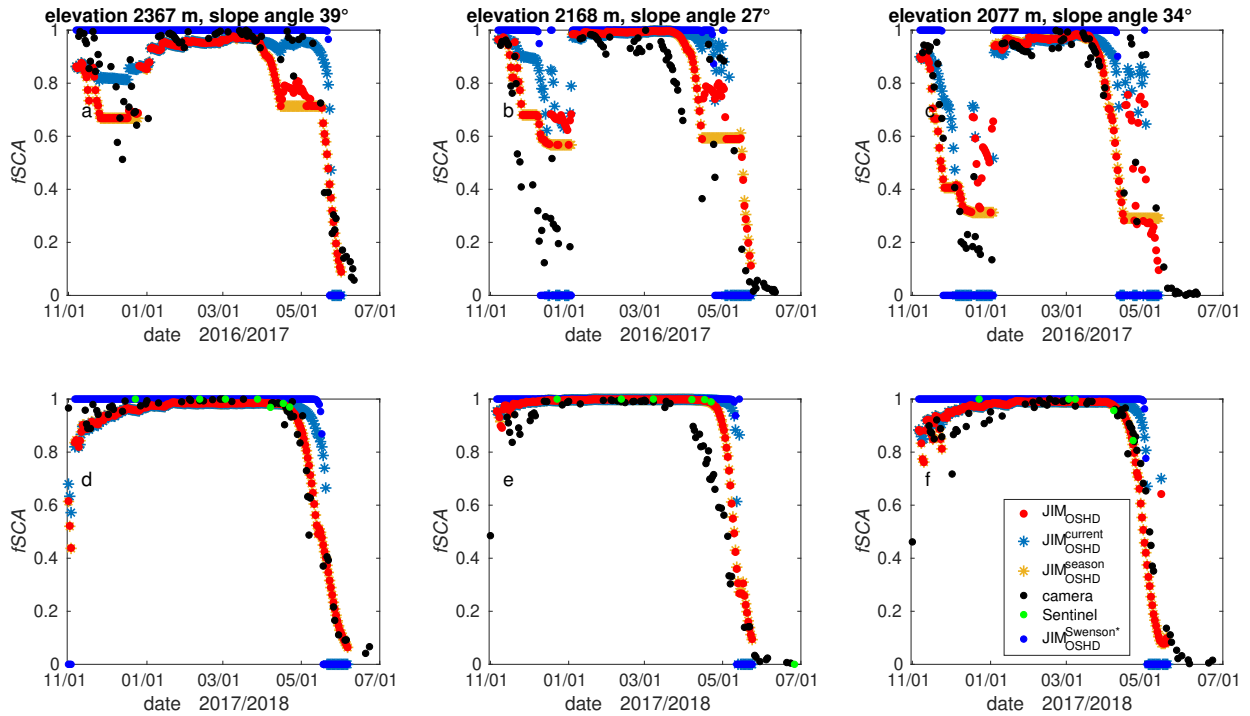
Figure 8. Modelled, camera- and Sentinel-derived $fSCA$ for the three 1 km grid cells within the field of view of the camera for two seasons: (a to c) winter 2017, (d to f) winter 2018.

. Note that, only for illustration, we here also show camera- and Sentinel-derived $fSCA$ (black and green dots) for grid cells with modelled $HS < 5$ cm.

4.3 Evaluation with $fSCA$ from Sentinel-2 snow products

Overall, modelled $fSCA$ using JIM$_{OSHD}$ compared well with Sentinel-derived $fSCA$ throughout the season (I in Table 5). To investigate the elevation-dependent differences between modelled and Sentinel-derived $fSCA$ in more detail, we binned the data in 250 m elevation bands for each day throughout the entire season (Figure 9). To estimate the end of the accumulation (1 April 2018) and ablation season (30 June 2018), we used the spatial mean HS (solid black line at bottom of Figure 9). Overall, differences in performance between the accumulation and the ablation period were small (I in Table 5). However, there were marked differences with elevation throughout the season. Up to the end of the accumulation period, the largest differences between modelled and Sentinel-derived $fSCA$ were at elevations lower than 1500 m, whereas at elevations above around 3000 m the agreement was good (Figure 9a). During the ablation period, most of the snow at lower elevations was gone, and modelled $fSCA$ was generally larger than Sentinel-derived $fSCA$ at higher elevations (> 2500 m), in particular towards the end of the ablation season. During the summer (30 June to 30 August 2018), i.e. after the end of the ablation season, modelled $fSCA$ was larger than Sentinel-derived $fSCA$ at the highest elevations (> 3500 m) whereas between the snow line and these highest elevations, modelled $fSCA$ was generally lower.

17
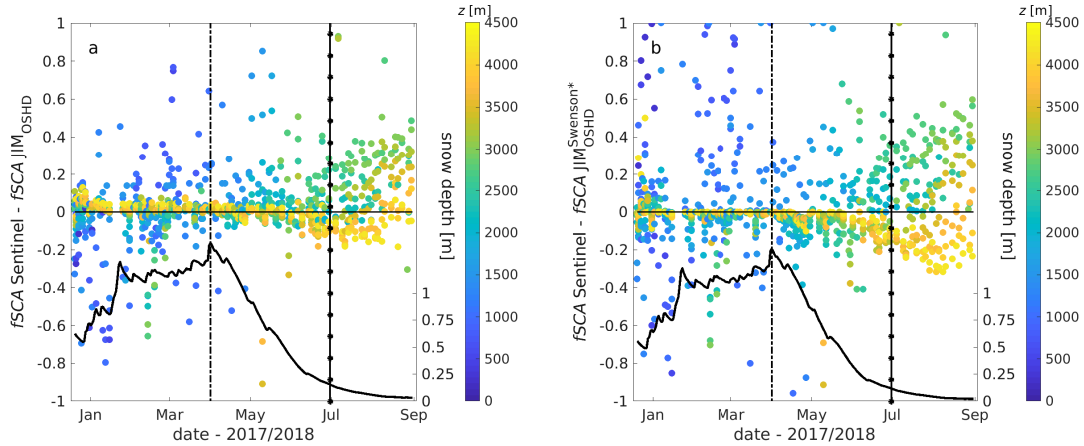
Figure 9. Difference between Sentinel-derived and modelled $fSCA$ for Switzerland as function of date and elevation z (in 250 m elevation bins) for available satellite dates for (a) JIM_{OSHD} and (b) $\text{JIM}_{\text{OSHD}}^{\text{Swenson*}}$. Daily spatial mean snow depth HS is also shown (solid black line). The vertical lines indicate the dates for the end of accumulation (dashed) and ablation (line with stars) season.

345 Given the high temporal resolution of the Sentinel-derived $fSCA$ data set, we again evaluated the $fSCA$ algorithm simplifications and $\text{JIM}_{\text{OSHD}}^{\text{Swenson*}}$ (cf. Table 1). Compared to our seasonal implementation, the overall performance values of the $fSCA$ algorithm simplifications were similar, except for $\text{JIM}_{\text{OSHD}}^{\text{curr}}$ and $\text{JIM}_{\text{OSHD}}^{\text{Swenson*}}$ (Table 5). Modelled $fSCA$ values with $\text{JIM}_{\text{OSHD}}^{\text{curr}}$ and $\text{JIM}_{\text{OSHD}}^{\text{Swenson*}}$ were generally larger than Sentinel-derived $fSCA$, resulting in larger MPE values with the largest ones for $\text{JIM}_{\text{OSHD}}^{\text{Swenson*}}$ (compare I, III and V in Table 5). This is also clearly reflected in the elevation-dependent differences between

350 $fSCA$ using $\text{JIM}_{\text{OSHD}}^{\text{Swenson*}}$ and Sentinel-derived $fSCA$ throughout the season (Figure 9b).

5 Discussion

5.1 Fractional snow-covered area $fSCA$ algorithm

Our seasonal $fSCA$ algorithm is based on the closed-form $fSCA$ parameterization of Helbig et al. (2015a) (Eq. 1) and combines two statistical parameterizations for σ_{HS} together with a tracking method to account for changes in maximum snow

355 depth and precipitation events. The algorithm is modular, meaning that individual parts can easily be complemented or replaced with new parameterizations e.g. for $fSCA_{\text{nsnow}}$. Overall, our algorithm only requires subgrid cell summer terrain parameters, which are a slope related parameter and the terrain correlation length, and tracking snow information.

We evaluated the performance of our seasonal $fSCA$ implementation in Switzerland. We could not explicitly evaluate the performance for completely flat grid cells, i.e. grid cells with a subgrid mean slope angle of zero. After removing rivers/lakes,

360 we only had five 1 km grid cells for Switzerland with a subgrid mean slope angle of zero, i.e. 0.01 % of all grid cells. For these grid cells, using $\sigma_{HS}^{\text{Helbig}}$ (Eq. 3) always results in a $fSCA$ of one. As a first approach, we therefore proposed to use $\sigma_{HS}^{\text{Egli}}$ (Eq.

Table 5. Performance measures for (I) modelled $fSCA$ using JIM_{OSHD} and Sentinel-retrieved $fSCA$ for the winter seasons 2018 for all valid 1 km grid cells of Switzerland and for all dates (20 December 2017 to 30 June 2018), for the accumulation period (20 December to 1 April) and for the ablation period (1 April to 30 June), and (II to V) for all JIM modelled $fSCA$ versions (for details see Table 1), namely for JIM_{OSHD}, JIM_{OSHD}^{season}, JIM_{OSHD}^{curr}, $JIM_{OSHD}^{allHelbig}$ and $JIM_{OSHD}^{Swenson*}$.

$fSCA$ vs Sentinel-2	NRMSE	RMSE	MPE
	[%]		[%]
I JIM_{OSHD}			
all dates	12	0.11	0.4
accumulation period	11	0.11	0.3
ablation period	14	0.12	0.5
II JIM_{OSHD}^{season}			
all dates	12	0.12	0.4
accumulation period	11	0.11	0.3
ablation period	14	0.12	0.5
III JIM_{OSHD}^{curr}			
all dates	14	0.13	-0.8
accumulation period	11	0.11	0.1
ablation period	18	0.16	-2.4
IV $JIM_{OSHD}^{allHelbig}$			
all dates	12	0.11	0.3
accumulation period	11	0.11	0.2
ablation period	14	0.12	0.5
V $JIM_{OSHD}^{Swenson*}$			
all dates	18	0.17	-1.8
accumulation period	17	0.16	-0.7
ablation period	21	0.19	-3.6

4). Although we see no reason why our $fSCA$ algorithm could not be used in other geographic region, it remains unclear at this point if our seasonal $fSCA$ implementation can also be used in flat regions.

We used $\sigma_{HS}^{\text{Egli}}$ (Eq. 4), which does not account for subgrid topography, to derive $fSCA_{\text{nsnow}}$. We did this to account for uniform blanketing after a snowfall, i.e. to account for possible increases in $fSCA$ after a recent snowfall. When substituting $\sigma_{dHS}^{\text{Egli}}$ by $\sigma_{dHS}^{\text{Helbig}}$ in Eq. (6) and (7) (JIM$_{\text{OSHD}}^{\text{allHelbig}}$, cf. Table 1), the overall performance was very similar (Table 4 and 5). Thus, while applying $\sigma_{dHS}^{\text{Egli}}$ might not describe the true spatial new snow distribution in mountainous terrain, the formulation is simple and is therefore used here as a first approach. Based on the modular algorithm setup, different closed-form $fSCA$ parameterizations can be applied in our seasonal algorithm, e.g. for a flat grid cell or for $fSCA_{\text{nsnow}}$ (for some empirical examples cf. Essery and Pomeroy, 2004).

5.2 Evaluation

5.2.1 Evaluation with $fSCA$ from fine-scale HS maps

The evaluation of the seasonal $fSCA$ algorithm with $fSCA$ from fine-scale HS maps showed that overall the model performed well, especially at PoW(I in Table 3). Modelled $fSCA$ using JIM$_{\text{OSHD}}^{\text{Swenson*}}$, on the other hand, generally overestimated $fSCA$ (MPE< 0). This algorithm inter-comparison shows that the seasonal $fSCA$ evolution is better captured by JIM$_{\text{OSHD}}$, most likely because the JIM$_{\text{OSHD}}^{\text{Swenson*}}$ model does not sufficiently account for the high spatial variability in snow distribution in complex terrain.

During accumulation at higher elevations, modelled $fSCA$ using JIM$_{\text{OSHD}}$ overestimated ADS-derived $fSCA$, even though modelled HS agreed reasonably well with the measurements (Figure 4a and 6a). We also used a different model configuration (JIM$_{\text{OSHD}}^{\text{allHelbig}}$ in Table 1), yet $fSCA$ values did not substantially change for the accumulation date [not shown]. Based on this we assume that both σ_{HS} parameterizations cannot sufficiently describe snow redistribution during accumulation, likely due to periods with strong winds following snowfall. The description of σ_{HS} during the accumulation period thus needs to be improved. This will, however, require more than one spatial HS data set during accumulation.

At PoW and during the ablation season, JIM$_{\text{OSHD}}$ mostly underestimated $fSCA$ compared to $fSCA$ from fine-scale HS maps, without a clear elevation trend (Figures 4 and 5). Discrepancies between modelled and measured HS, on the other hand, generally increased with elevation (Figure 6 and 7). Obviously for larger snow depth, correctly modelling HS has little effect on $fSCA$, The overall underestimated modelled $fSCA$ values were likely a consequence of the HS threshold of 0 m we used to decide whether a 2 or 5 m grid cell was snow-covered or not. In reality, due to measurement uncertainties, both small positive or negative measured HS values can still be associated with snow free areas. When arbitrarily increasing the HS threshold to $\pm$ 10 cm for the ALS-data, modelled 1 km $fSCA$ values were rather larger than the measurements [not shown]. This is not contradictory, but emphasizes the need to accurately model HS along snow lines, where small inaccuracies in HS can have large impacts on $fSCA$. For instance, during early ablation modelled as well as measured $fSCA$ are larger in the lowest elevation bin than at higher elevations (cf. Fig. 4c). Unfortunately, we currently do not have detailed snow observations available to define robust HS threshold values which take into account the different points in time of the season as well as

395 the influence of terrain and ground cover. However, the overall good agreement between Sentinel- and ALS-derived $fSCA$ (Figure 5 and III in Table 3) provides some confidence in the fine-scale HS data-derived $fSCA$ used here to evaluate modelled $fSCA$.

The two benchmark $fSCA$ models based on Eq. (1) using measured rather than modelled HS data ($fSCA_{\text{curr}}^{\text{measured}}$ and $fSCA_{\text{PoW}}^{\text{measured}}$) generally showed similar trends as HS-derived and modelled $fSCA$ (Figure 4 and 5). At PoW, $fSCA_{\text{curr}}^{\text{measured}}$

400 agreed less well with measured $fSCA$ than our seasonal implementation (cf. Figure 4b and 5a). This may indicate uncertainties in the empirical $fSCA$ parameterization (Eq. 1), which requires further investigation of spatial HS data sets during accumulation. During ablation, we expected that $fSCA_{\text{PoW}}^{\text{measured}}$ would be closer to measured $fSCA$ than $fSCA_{\text{curr}}^{\text{measured}}$, which was however not the case (cf. Figure 4c and 5b). Since the true PoW date is elevation and aspect dependent, we cannot assume that one date for PoW is representative for the entire catchment, covering several hundred of square kilometers and large ele-

405 vation gradients. Thus, measured σ_{HS} at the date we defined as PoW, might not have been representative for the true $\sigma_{HS_{\max}}$ in each grid cell as required by Eq. (5). Besides possible uncertainties in the empirical $fSCA$ parameterization (Eq. 1), we assume this is the main reason why these two benchmark models using measured HS data did not outperform our seasonal implementation. Overall, these comparisons emphasize the need for tracking snow information per grid cell, as is done by our seasonal $fSCA$ algorithm.

410 **5.2.2 Evaluation with camera-derived $fSCA$**

The evaluation with fine-scale HS maps revealed overall good model performance at six points in time. It was however not possible to comprehensively evaluate the performance over the season. For this, we used daily camera-derived $fSCA$, showing that the modelled seasonal $fSCA$ trend was mostly in line with observations (Figure 8).

Model performance compared to the camera-derived $fSCA$ values was overall worse than when comparing to HS-derived

415 $fSCA$ (e.g. NRMSE of 21 % for I in Table 4 compared to NRMSE of 7 % for I in Table 3). Since the higher temporal resolution of the camera data set leads to the largest spread in $fSCA$ values compared to the other two data sets (cf. Table 2 and Fig. 3), a larger portion of intermediate $fSCA$ values (e.g. close to the snow line) are included which are generally more difficult to model correctly than $fSCA$ values close to one. The poorer model performance is however likely also be due to the overall lower accuracy of camera-derived $fSCA$. For instance, the projection of the 2D-camera image to a 3D DEM may

420 introduce errors and distortions. Furthermore, when deriving $fSCA$ from camera images, clouds/fog and uneven illumination, for instance due to shading or partial cloud cover, may deteriorate the accuracy (e.g. Farinotti et al., 2010; Fedorov et al., 2016; Härer et al., 2016; Portenier et al., 2020). Another factor affecting the performance measures was the threshold for the number of valid fine-scale data per 1 km grid cell. When aggregating to 1 km $fSCA$ maps for the Sentinel-derived values, we required at least 50 % valid fine-scale data. This requirement could not be met for camera-derived $fSCA$, as the projected fractions

425 of the camera FOV on the 1 km model grid cells were only 9 %, 13 % and 14 %. This is reflected in the better agreement between modelled and Sentinel-derived $fSCA$ than between camera- and Sentinel-derived $fSCA$ (NRMSE of 2 % versus 12 % in Table 4). Finally, as the camera was installed at valley bottom, steep slope sections cover larger areas of the FOV, while flatter slope parts remain invisible. This likely lead to underestimated $fSCA$ values. On the other hand, valid Sentinel-derived

$fSCA$ has a much lower temporal resolution and did not cover the entire ablation period. Instead, Sentinel-derived $fSCA$ was often available throughout the period when $fSCA$ was rather close to one (cf. Figure 8d,e). Thus, while there is likely more uncertainty in camera-derived $fSCA$, the high temporal resolution of this product still provides valuable information on model performance throughout the season.

We used the camera-derived $fSCA$ to also evaluate simplifications of our seasonal $fSCA$ algorithm as well as $\text{JIM}_{\text{OSHD}}^{\text{Swenson*}}$ (Table 1). Compared to our seasonal $fSCA$ implementation, the more simple implementations did not capture the seasonal variation as well (Figure 8). With $\text{JIM}_{\text{OSHD}}^{\text{curr}}$, the start of the ablation season was delayed, and the ablation season was also considerably shortened, by up to 21 days. In this respect, the results for $\text{JIM}_{\text{OSHD}}^{\text{Swenson*}}$ were very similar, as overall the increases and decreases of $fSCA$ were very steep, leading to shortened snow seasons and poorer performances (cf. Table 4). In principle, $\text{JIM}_{\text{OSHD}}^{\text{curr}}$ considers each day as PoW, leading to rapid changes in $fSCA$, in particular when HS values are low (i.e. early accumulation or ablation season). In $\text{JIM}_{\text{OSHD}}^{\text{season}}$, the seasonal maximum value of HS was additionally tracked, substantially improving the seasonal $fSCA$ trend, in particular during the ablation season. However, changes in $fSCA$ due to snowfall events were still not captured well with this implementation, showing that our new snow tracking algorithm further improves the overall model performance. Since the impact of using $\text{JIM}_{\text{OSHD}}^{\text{allHelbig}}$ on modelled $fSCA$ is mainly restricted to snowfall following melt periods, overall performances were very similar to JIM_{OSHD} (cf. Table 4 and 5). This again indicates that the description of σ_{HS} following snowfall events requires further investigation.

5.2.3 Evaluation with Sentinel-derived $fSCA$

By including Sentinel-derived $fSCA$ in our evaluation, we added a data set with both a high temporal resolution and a much larger spatial coverage (cf. Table 2). The Sentinel-derived $fSCA$ data set comprised about 217'000 1 km grid cells covering a wide range in terrain elevations, slope angles and terrain aspects.

For the investigated winter season, results showed an overall good seasonal agreement across Switzerland, though there was some elevation-dependent scatter (Figure 9a). Discrepancies during accumulation occurred mostly along the snowline at lower elevations, where lower spatial HS values as well as more cloudy weather prevail during accumulation. Both can lead to inaccurate modelled and Sentinel-derived $fSCA$. Furthermore, we assume that some of the overestimations in modelled $fSCA$ at higher elevations during accumulation could also stem from underestimated σ_{HS} during periods when strong winds follow snowfall events, as was also observed in the HS data sets (Figure 4a and Section 5.2.1). The scatter at high elevations during ablation and summer likely originates from lower modelled $fSCA$ due to underestimated precipitation, as there are fewer AWS at high elevations for data assimilation in our model.

Performance measures were somewhat poorer as those from fine-scale HS maps (e.g. NRMSE of 12 % for Sentinel versus 7 % for $fSCA$ for HS data). Uncertainties introduced by reduced visibility in the snow products of Sentinel-2 are the most likely reason for this. Both, our camera- as well as the Sentinel-2 data set cover long time periods in higher temporal resolution, i.e. they include also periods under unfavorable weather conditions. On the contrary, clear sky dates were carefully selected for the on-demand high-quality data acquisitions from the air for our $fSCA$ data sets derived from fine-scale HS maps. Nevertheless,

the camera- as well as the Sentinel-2 data set enabled us to evaluate seasonal $fSCA$ model trends which would not have been possible from only six $fSCA$ data sets derived from HS data.

When evaluating the simplified $fSCA$ algorithms and $\text{JIM}_{\text{OSHD}}^{\text{Swenson*}}$, model performance measures were comparable to our seasonal implementation except for $\text{JIM}_{\text{OSHD}}^{\text{curr}}$ and $\text{JIM}_{\text{OSHD}}^{\text{Swenson*}}$ (Table 5), as was also the case for the comparison with camera-derived $fSCA$ (Table 4). For Sentinel- and camera-derived $fSCA$, the main reason is likely the limited availability of $fSCA$ data during or shortly after snowfall, due to bad visibility and clouds. Additionally, for the Sentinel-derived $fSCA$, local performance differences across Switzerland are likely averaged out. Nevertheless, $fSCA$ values when using $\text{JIM}_{\text{OSHD}}^{\text{Swenson*}}$ were overestimated compared to Sentinel-derived values (Figure 9b, and negative MPE for V in Table 5). Similar results were also observed when using $\text{JIM}_{\text{OSHD}}^{\text{curr}}$ (cf. negative MPE for III in Table 5). These biases are most likely related to the rather steep increases and decreases of modelled $fSCA$ over the season, as we also observed with the camera-derived $fSCA$ (Figure 8). We further assume that overestimated $fSCA$ using $\text{JIM}_{\text{OSHD}}^{\text{Swenson*}}$ at higher elevations, due to underestimating spatial snow depth variability in complex terrain, may have compensated for other modelled $fSCA$ error sources (e.g. from underestimated precipitation input at these elevations) leading to an overall lower bias at higher elevations during accumulation compared to our $fSCA$ implementation. Finally, note that the scatter above zero between Sentinel-derived and $\text{JIM}_{\text{OSHD}}^{\text{Swenson*}}$ $fSCA$ (Figure 9b) almost disappears when we neglect all 1 km domains with modelled $HS < 5$ cm using $\text{JIM}_{\text{OSHD}}^{\text{Swenson*}}$ [not shown]. While the overall NRMSE values for $\text{JIM}_{\text{OSHD}}^{\text{Swenson*}}$ are then comparable to our seasonal implementation (e.g. NRMSE of 12 % for all dates instead of 18 %; cf. V in Table 5), it reveals the overall overestimation of $\text{JIM}_{\text{OSHD}}^{\text{Swenson*}}$ (e.g. increased negative MPE of -4.1 % for all dates instead of -1.8 %). Clearly, our seasonal $fSCA$ implementation is better suited to more realistically represent seasonal changes in mountainous terrain, in particular following snowfall and during the ablation period.

6   Conclusions

We presented a seasonal fractional snow-covered area ($fSCA$) algorithm based on the $fSCA$ parameterization of Helbig et al. (2015b, 2021). The seasonal algorithm is based on tracking HS and SWE values accounting for alternating snow accumulation and melt events. Two empirical parameterizations were used to describe the spatial snow depth distribution, one for mountainous terrain and one not accounting for subgrid topography. An implementation in a multilayer energy balance snow cover model system (JIM_{OSHD}; JIM, JULES investigation model (Essery et al., 2013)) allowed us to evaluate seasonally modelled $fSCA$ for Switzerland.

Compiling independent $fSCA$ data sets with different spatiotemporal characteristics enabled a thorough analysis of the seasonal $fSCA$ algorithm in mountainous terrain of daily 1km-$fSCA$ values. While the evaluation with the three data sets showed overall good seasonal performance, each of the evaluation data sets allowed drawing specific conclusions. The evaluation with fine-scale spatial HS-derived $fSCA$ showed that HS uncertainties along the snow line likely contributed most to underestimation of $fSCA$ during ablation and PoW, emphasizing the need to accurately model HS along snow lines. The camera-derived $fSCA$ data set, with the highest temporal resolution confirmed the need for tracking HS over the season as well as accounting for intermediate snowfalls to avoid a delayed melt start and a drastic shortening of the ablation season. The

Sentinel-derived $fSCA$ data set, with the largest spatial coverage together with a rather high temporal resolution, demonstrated that the seasonal $fSCA$ algorithm performs well across a range of elevations, slope angles, terrain aspects and snow regimes. This comparison showed that there were some differences at low elevation or along the snowline coinciding with low HS, while discrepancies occurred mostly at high elevations towards the end of the season, respectively during summer.

Overall, NRMSE's for seasonally modelled $fSCA$ increased from 7 % for HS data-derived $fSCA$, to 12 % for Sentinel-derived $fSCA$ and to 21 % for camera-derived $fSCA$. While the large variation in performance measures is likely tied to the various temporal and spatial resolutions of the data sets and measurement uncertainties, it also demonstrates the difficulties in drawing conclusions when evaluating a model algorithm with evaluation data from different acquisition platforms. Nevertheless, this comparison with data covering a wide range of spatiotemporal scales allowed us to obtain a comprehensive overview of the strength and weaknesses of our seasonal $fSCA$ implementation. We are not aware of any seasonal $fSCA$ implementation that has been evaluated in such detail by exploiting independent HS and snow product data sets in high spatial and temporal resolution.

By implementing the $fSCA$ parameterizations applied in CLM5.0 (Lawrence et al., 2018) in JIM$_{\text{OSHD}}$, we also evaluated modelled $fSCA$ using JIM$_{\text{OSHD}}^{\text{Swenson*}}$. This showed that our seasonal $fSCA$ algorithm captures the seasonal variation best, and that seasonal variation in JIM$_{\text{OSHD}}^{\text{Swenson*}}$ was limited. JIM$_{\text{OSHD}}^{\text{Swenson*}}$ resulted in often overestimated $fSCA$ values, likely because the high spatial variability in snow depth distribution in complex terrain is not sufficiently described.

The implementation of the seasonal $fSCA$ algorithm in a model only requires subgrid terrain parameters from a fine-scale summer DEM in combination with tracking HS and SWE for coarse grid cells. The algorithm is set up such that improvements or adaptations of individual algorithm parts can easily be implemented. The PoW $fSCA$ parameterization of Helbig et al. (2015b) forms the centerpiece of the presented seasonal $fSCA$ algorithm. The recent re-evaluation with various spatial PoW snow depth data sets from 7 geographic regions showed an overall NRMSE of only 2 % (Helbig et al., 2021). This detailed evaluation at PoW in different geographic regions together with the seasonal assessment with the three $fSCA$ data pools presented here, suggests that the seasonal $fSCA$ algorithm may also be used in other geographic regions. However, further investigations, once more spatial HS data sets before and after snowfalls in complex topography become available, would be advantageous for improvements of our seasonal $fSCA$ algorithm, especially during the accumulation period.

References

Andreadis, K. M. and Lettenmaier, D. P.: Assimilating remotely sensed snow observations into a macroscale hydrology model, Adv. Water Resour., 29, 872–886, 2006.

Baba, M. W., Gascoin, S., and Hanich, L.: Assimilation of Sentinel-2 Data into a Snowpack Model in the High Atlas of Morocco, Remote Sens., 10, 1982, https://doi.org/10.3390/rs10121982, 2018.

Bellaire, S. and Jamieson, B.: Forecasting the formation of critical snow layers using a coupled snow cover and weather model, Cold. Reg. Sci. Technol., 94, 37–44, 2013.

Bühler, Y., Marty, M., Egli, L., Veitinger, J., Jonas, T., Thee, P., and Ginzler, C.: Snow depth mapping in high-alpine catchments using digital photogrammetry, Cryosphere, 9, 229–243, https://doi.org/10.5194/tc-9-229-2015, 2015.

Cluzet, B., Revuelto, J., Lafaysse, M., Tuzet, F., Cosme, E., Picard, G., Arnaud, L., and Dumont, M.: Towards the assimilation of satellite reflectance into semi-distributed ensemble snowpack simulations, Cold Regions Science and Technology, 170, 102 918, https://doi.org/https://doi.org/10.1016/j.coldregions.2019.102918, 2020.

Doms, G., Förstner, J., Heise, E., Herzog, H. J., Mironov, D., Raschendorfer, M., Reinhardt, T., Ritter, B., Schrodin, R., Schulz, J. P., and Vogel, G.: A Description of the Nonhydrostatic Regional COSMO Model, Part II: Physical Parameterization, LM F90 4.20 38, Consortium for Small-Scale Modelling,Printed at Deutscher Wetterdienst,63004 Offenbach,Germany, 2011.

Douville, H., Royer, J.-F., and Mahfouf, J.-F.: A new snow parameterization for the Météo-France climate model Part II: validation in a 3-D GCM experiment, Climate Dynamics, 1, 37–52, 1995.

Drusch, M., Del Bello, U., Carlier, S., Colin, O., Fernandez, V., Gascon, F., Hoersch, B., Isola, C., Laberinti, P., Martimort, P., et al.: Sentinel-2: ESA's optical high-resolution mission for GMES operational services, Remote Sensing of Environment, 120, 25–36, 2012.

Egli, L. and Jonas, T.: Hysteretic dynamics of seasonal snow depth distribution in the Swiss Alps, Geophys. Res. Lett., 36, 2009.

Essery, R.: Large-scale simulations of snow albedo masking by forests, Geophys. Res. Lett., 40, 5521–5525, https://doi.org/10.1002/grl.51008, 2013.

Essery, R. and Pomeroy, J.: Implications of spatial distributions of snow mass and melt rate for snow-cover depletion: theoretical considerations, Ann. Glaciol., 38, 2004.

Essery, R., Morin, S., Lejeune, Y., and Ménard, C. B.: A comparison of 1701 snow models using observations from an alpine site, Adv. Water Resour., 55, 131–148, 2013.

Farinotti, D., Magnusson, J., Huss, M., and Bauder, A.: Snow accumulation distribution inferred from time-lapse photography and simple modelling, Hydrological Processes, 24, 2087–2097, https://doi.org/10.1002/hyp.7629, 2010.

Fedorov, R., Camerada, A., Fraternali, P., and Tagliasacchi, M.: Estimating Snow Cover From Publicly Available Images, IEEE Transactions on Multimedia, 18, 1187–1200, https://doi.org/10.1109/TMM.2016.2535356, 2016.

Gascoin, S., Hagolle, O., Huc, M., Jarlan, L., Dejoux, J.-F., Szczypta, C., Marti, R., and Sánchez, R.: A snow cover climatology for the Pyrenees from MODIS snow products, Hydrol. Earth Syst. Sci., 19, 2337–2351, 2015.

Gascoin, S., Grizonnet, M., Bouchet, M., Salgues, G., and Hagolle, O.: Theia Snow collection: high resolution operational snow cover maps from Sentinel-2 and Landsat-8 data, Earth Syst. Sci. Data, pp. 493–514, https://doi.org/10.5194/essd-11-493-2019, 2019.

Griessinger, N., Seibert, J., Magnusson, J., and Jonas, T.: Assessing the benefit of snow data assimilation for runoff modeling in Alpine catchments, Hydrol. Earth Syst. Sci., 20, 3895–3905, 2016.

565 Griessinger, N., Schirmer, M., Helbig, N., Winstral, A., Michel, A., and Jonas, T.: Implications of observation-enhanced energy-balance snowmelt simulations for runoff modeling of Alpine catchments, Advances in Water Resources, 133, 103 410, https://doi.org/10.1016/j.advwatres.2019.103410, 2019.

Hall, D. K., Riggs, G. A., and Salomonson, V. V.: Development of methods for mapping global snow cover using moderate resolution imaging spectroradiometer data, Remote Sensing of Environment, 54, 127 – 140, https://doi.org/https://doi.org/10.1016/0034-4257(95)00137-P, 570 1995.

Härer, S., Bernhardt, M., and Schulz, K.: PRACTISE – Photo Rectification And ClassificaTIon SoftwarE (V.2.1), Geoscientific Model Development, 9, 307–321, https://doi.org/10.5194/gmd-9-307-2016, 2016.

Helbig, N., van Herwijnen, A., and Jonas, T.: Forecasting wet-snow avalanche probability in mountainous terrain, Cold Reg. Sci. Technol., 120, 219 – 226, https://doi.org/10.1016/j.coldregions.2015.07.001, 2015a.

575 Helbig, N., van Herwijnen, A., Magnusson, J., and Jonas, T.: Fractional snow-covered area parameterization over complex topography, Hydrol. Earth Syst. Sci., 19, 1339–1351, https://doi.org/10.5194/hess-19-1339-2015, 2015b.

Helbig, N., Bühler, Y., Eberhard, L., Deschamps-Berger, C., Gascoin, S., Dumont, M., Revuelto, J., Deems, J. S., and Jonas, T.: Fractional snow-covered area: Scale-independent peak of winter parameterization, The Cryosphere, 15, 615–632, https://doi.org/doi.org/10.5194/tc-15-615-2021, 2021.

580 Horton, S. and Jamieson, B.: Modelling hazardous surface hoar layers across western Canada with a coupled weather and snow cover model, Cold. Reg. Sci. Technol., 128, 22–31, 2016.

Huang, C., Newman, A., Clark, M. P., Wood, A. W., and Zheng, X.: Evaluation of snow data assimilation using the ensemble Kalman filter for seasonal streamflow prediction in the western United States, Hydrol. Earth Syst. Sci., 21, 635–650, https://doi.org/10.1029/JB094iB06p07491, 2017.

585 Lawrence, D., Fisher, R., Koven, C., Oleson, K., Swenson, S., and Vertenstein, M.: Technical Description of version 5.0 of the Community Land Model (CLM), https://www.cesm.ucar.edu/models/cesm2/land/CLM50_Tech_Note.pdf, [Online; accessed 31-March-2018], 2018.

López-Moreno, J. I., Revuelto, J., Alonso-Gonzáles, E., Sanmiguel-Vallelado, A., Fassnacht, S. R., Deems, J., and Morán-Tejeda, E.: Using very long-range Terrestrial Laser Scanning to Analyze the Temporal Consistency of the Snowpack Distribution in a High Mountain Environment, J. Mt. Sci., 14, 823–842, 2017.

590 Luce, C. H., Tarboton, D. G., and Cooley, K. R.: Sub-grid parameterization of snow distribution for an energy and mass balance snow cover model, Hydrol. Process., 13, 1921–1933, 1999.

Magand, C., Ducharne, A., Moine, N. L., and Gascoin, S.: Introducing Hysteresis in Snow Depletion Curves to Improve the Water Budget of a Land Surface Model in an Alpine Catchment, J. Hydrometeor., 15, 631–649, https://doi.org/10.1175/JHM-D-13-091.1, 2014.

Magnusson, J., Gustafsson, D., Hüsler, F., and Jonas, T.: Assimilation of point SWE data into a distributed snow cover model comparing two 595 contrasting methods, Water Resour. Res., 50, 7816–7835, 2014.

Magnusson, J., Wever, N., Essery, R., Helbig, N., Winstral, A., and Jonas, T.: Evaluating snow models with varying process representations for hydrological applications, Water Resour. Res., 51, 2707–2723, https://doi.org/10.1002/2014WR016498, 2015.

Marty, M., Bühler, Y., and Ginzler, C.: Snow Depth Mapping, https://doi.org/10.16904/envidat.62, https://www.envidat.ch/dataset/snow-depth-mapping, 2019.

600 Masson, T., Dumont, M., Mura, M., Sirguey, P., Gascoin, S., Dedieu, J.-P., and Chanussot, J.: An Assessment of Existing Methodologies to Retrieve Snow Cover Fraction from MODIS Data, Remote Sensing, 10, 619, https://doi.org/10.3390/rs10040619, 2018.

Mazzotti, G., Currier, W. R., Deems, J. S., Pflug, J. M., Lundquist, J. D., and Jonas, T.: Revisiting Snow Cover Variability and Canopy Structure Within Forest Stands: Insights From Airborne Lidar Data, Water Resour. Res., 55, 6198–6216, 2019.

Mudryk, L., Santolaria-Otín, M., Krinner, G., Ménégoz, M., Derksen, C., Brutel-Vuilmet, C., Brady, M., and Essery, R.: Historical Northern Hemisphere snow cover trends and projected changes in the CMIP-6 multi-model ensemble, The Cryosphere Discussions, 2020, 1–35, https://doi.org/10.5194/tc-2019-320, 2020.

Nagler, T., Rott, H., Malcher, P., and Müller, F.: Assimilation of meteorological and remote sensing data for snowmelt runoffforecasting, Remote Sens. Environ., 112, 1408–1420, 2008.

Nitta, T., Yoshimura, K., Takata, K., O'ishi, R., Sueyoshi, T., Kanae, S., Oki, T., Abe-Ouchi, A., and Liston, G. E.: Representing Variability in Subgrid Snow Cover and Snow Depth in a Global Land Model: Offline Validation, J. Climate, 27, 3318–3330, https://doi.org/10.1175/JCLI-D-13-00310.1, 2014.

Niu, G. Y. and Yang, Z. L.: An observation-based formulation of snow cover fraction and its evaluation over large North American river basins, J. Geophys. Res., 112, https://doi.org/10.1029/2007JD008674, 2007.

Painter, T., Berisford, D., Boardman, J., Bormann, K., Deems, J., Gehrke, F., Hedrick, A., Joyce, M., Laidlaw, R., Marks, D., Mattmann, C., Mcgurk, B., Ramirez, P., Richardson, M., Skiles, S. M., Seidel, F., and Winstral, A.: The Airborne Snow Observatory: fusion of scanning lidar, imaging spectrometer, and physically-based modeling for mapping snow water equivalent and snow albedo, Remote Sens. Environ., 184, 139–152, https://doi.org/10.1016/j.rse.2016.06.018, 2016.

Painter, T. H., Rittger, K., McKenzie, C., Slaughter, P., Davis, R. E., and Dozier, J.: Retrieval of subpixel snow covered area, grain size, and albedo from MODIS, Remote Sensing of Environment, 113, 868 – 879, https://doi.org/https://doi.org/10.1016/j.rse.2009.01.001, http://www.sciencedirect.com/science/article/pii/S0034425709000029, 2009.

Parajka, J. and Blöschl, G.: Validation of MODIS snow cover images over Austria, Hydrol. Earth Syst. Sci. Discuss., 3, 1569–1601, 2006.

Portenier, C., Hüsler, F., Härer, S., and Wunderle, S.: Towards a webcam-based snow cover monitoring network: methodology and evaluation, Cryosphere, 14, 1409–1423, https://doi.org/10.5194/tc-14-1409-2020, 2020.

Revuelto, J., López-Moreno, J. I., Azorín-Molina, C., and Vicente-Serrano, S.: Topographic control of snowpack distribution in a small catchment in the central Spanish Pyrenees: intra- and inter-annual persistence, Cryosphere, 6, 1989–2006, 2014.

Riboust, P., Thirel, G., Le Moine, N., and Ribstein, P.: Revisiting a simple degree-day model for integrating satellite data: implementation of SWE-SCA hystereses, J. Hydrol. Hydromech., 67, 70–81, 2019.

Roesch, A., Wild, M., Gilgen, H., and Ohmura, A.: A new snow cover fraction parameterization for the ECHAM4 GCM, Clim. Dyn., 17, 933–946, 2001.

Salvatori, R., Plini, P., Giusto, M., Valt, M., Salzano, R., Montagnoli, M., Cagnati, A., Crepaz, G., and Sigismondi, D.: Snow cover monitoring with images from digital camera systems, Ital. J. Remote. Sens., 43, https://doi.org/10.5721/ItJRS201143211, 2011.

Schirmer, M. and Lehning, M.: Persistence in intra-annual snow depth distribution: 2. Fractal analysis of snow depth development, Water Resour. Res., 47, https://doi.org/10.1029/2010WR009429, 2011.

Schirmer, M., Wirz, V., Clifton, A., and Lehning, M.: Persistence in intra-annual snow depth distribution: 1. Measurements and topographic control, Water Resour. Res., 47, 2011.

Skaugen, T. and Melvold, K.: Modeling the snow depth variability with a high-resolution lidar data set and nonlinear terrain dependency, Water Resour. Res., 55, 9689–9704, https://doi.org/10.1029/2019WR025030, 2019.

Su, H., Yang, Z. L., Niu, G. Y., and Dickinson, R. E.: Enhancing the estimation of continental-scale snow water equivalent by assimilating MODIS snow cover with the ensemble Kalman filter, J. Geophys. Res., 113, 2008.

640   Swenson, S. C. and Lawrence, D. M.: A new fractional snow-covered area parameterization for the Community Land Model and its effect on the surface energy balance, Journal of Geophysical Research: Atmospheres, 117, https://doi.org/10.1029/2012JD018178, 2012.

Thirel, G., Salamon, P., Burek, P., and Kalas, M.: Assimilation of MODIS snow cover area data in a distributed hydrological model using the particle filter, Remote Sensing, 5, 5825–5850, 2013.

van Herwijnen, A. and Schweizer, J.: Seismic sensor array for monitoring an avalanche start zone: design, deployment and preliminary

645   results, J. Glaciol., 57, 257–264, 2011.

van Herwijnen, A., Berthod, N., Simenhois, R., and Mitterer, C.: Using time-lapse photography in avalanche research, in: Proceedings of the International Snow Science Workshop, Grenoble, France, pp. 950–954, 2013.

Vionnet, V., Martin, E., Masson, V., Guyomarc'h, G., Naaim-Bouvet, F., Prokop, A., Durand, Y., and Lac, C.: Simulation of wind-induced snow transport and sublimation in alpine terrain using a fully coupled snowpack/atmosphere model, Cryosphere, 8, 395–415, 2014.

650   Yang, Z. L., Dickinson, R. E., Robock, A., and Vinnikov, K. Y.: On validation of the snow sub-model of the biosphere atmosphere transfer scheme with Russian snow cover and meteorological observational data, J. Climate, 10, 353–373, 1997.

Zaitchik, B. F. and Rodell, M.: Forward-Looking Assimilation of MODIS-Derived Snow-Covered Area into a Land Surface Model, Journal of Hydrometeorology, 10, 130 – 148, https://doi.org/10.1175/2008JHM1042.1, 2009.